resources

MDPI

Article

Chemistry of Hydrothermally Destabilized Rare-Metal and Radioactive Minerals in Deformed A-Type Granite in the Vicinity of Nugrus Shear Zone, South Eastern Desert, Egypt

Adel A. Surour [1,2,*], Amira M. El-Tohamy [3] and Gehad M. Saleh [3]

[1] Department of Geological Sciences, Faculty of Science, Galala University, New Galala City 43511, Egypt
[2] Geology Department, Faculty of Science, Cairo University, Giza 12613, Egypt
[3] Nuclear Materials Authority of Egypt, Maadi P.O. Box 530, Egypt; amira_eltohamy2011@yahoo.com (A.M.E.-T.); drgehad_m@yahoo.com (G.M.S.)
* Correspondence: adelsurour@hotmail.com or adel-surour@gu.edu.eg or adelsurour@cu.edu.eg

Abstract: In the Wadi Nugrus area, south Eastern Desert of Egypt, A-type granite is highly deformed in a prominent NW-SE trending shear zone, likely related to the Najd shear system. Deformation of this post-collisional leucogranite allows the propagation of hydrothermal alterations due to fluid circulation inside the so-called "Nugrus Shear Zone (NSZ)". This results in the remarkable destabilization of the magmatic dissemination of rare-metal and U-Th minerals in the granite. Relict magmatic minerals that survived destabilization are represented by (1) ferrocolumbite with 14–63–16.39 wt% FeO^t, (2) fresh igneous zircon, and (3) thorite. The destabilized ore minerals (hydrothermal) dominate over the fresh magmatic relict minerals. The former comprises the following: (1) altered columbite in the form of three distinct phases of niobates (fergusonite–petscheckite–uranopyrochlore), (2) altered thorite (Ce-bearing and P-F-rich), (3) betafite, (4) altered uranothorite, and (5) sulfides (mainly pyrite). It is evident that the destabilization of magmatic thorite can be distinguished into three stages of hydrothermal alteration, namely low-Zr Ce-bearing thorite (stage I), moderate-Zr Ce-bearing thorite (stage II), and high-Zr U-Nb-Y-bearing thorite (stage III). The two varieties of Ce-bearing thorite are sodic with 1.33–2.28 wt% and 1.51–1.80 wt% Na_2O, respectively, whereas the U-Nb-Y-bearing thorite is Na_2O-poor (0.06–0.07 wt%). Similarly, thorite in stages I and II are Ca-, P-, F-, and S-rich. Considerable P_2O_5 content (up to ~17 wt%) is reported in stage II Ce-bearing thorite, whereas stage III thorite is Si-rich (14.56–18.79 wt% SiO_2). Upon hydrothermal destabilization, the three niobate minerals replacing the dissemination of magmatic ferrocolumbite become enriched in UO_2 (up to 15.24 wt%, 7.86 wt%, and 10.88 wt%, respectively), and similarly, ThO_2 (up to 7.13 wt%, 5.71 wt%, and 9.52 wt%, respectively). Hydrothermal destabilization results in the complete dissolution of magmatic fluorite and phosphate minerals at pH = 2–7. This furnishes a source of Ca, P, Ce, Y, F, and Cl in the hydrothermal solution to destabilize/collapse the structure of magmatic ore minerals, particularly ferrocolumbite and thorite. Free elements in the hydrothermal solution are responsible for the crystallization of P- and F-rich Ce-bearing thorite minerals in three stages, as well as abnormal Y_2O_3 enrichment in three resulting niobates that contain up to 6.03 wt%, 2.93 wt%, and 2.65 wt%, respectively. The fresh undeformed Nugrus leucogranite is sulfide-poor. In contrast, sulfides are enriched in the deformed leucogranite inside the NSZ. Also, the intimate relationship of sulfides with destabilized rare-element minerals indicates the destabilization of these minerals during the hydrothermal stage under reduced conditions. Finally, the proposed paragenetic sequence suggests that most ore minerals are magmatic or hydrothermal primarily. In contrast, supergene minerals such as goethite, Fe-oxyhydroxide, altered betafite, and altered uranothorite are the least abundant.

Academic Editor: Jian Cao

Received: 20 August 2024
Revised: 11 December 2024
Accepted: 13 December 2024
Published: 26 December 2024

Citation: Surour, A.A.; El-Tohamy, A.M.; Saleh, G.M. Chemistry of Hydrothermally Destabilized Rare-Metal and Radioactive Minerals in Deformed A-Type Granite in the Vicinity of Nugrus Shear Zone, South Eastern Desert, Egypt. *Resources* **2025**, *14*, 4. https://doi.org/10.3390/resources14010004

Keywords: Nugrus shear zone; deformed A-type granite; magmatic dissemination; hydrothermal; supergene; destabilization; U-Th-rare metal ores

1. Introduction

In the context of the present research, rare-element ore minerals in the investigated granites comprise the following: (1) radionuclides, (2) rare metals, and (3) rare-earth elements (REEs). Fresh and altered rare-element minerals from the Nubian Shield in Egypt are an issue of expanding interest for regional and international researchers who focus on metallogenic provinces during the Neoproterozoic era. Such mineralizations are concentrated in the Eastern Desert of Egypt as a part of the Arabian–Nubian Shield (ANS) formed by Precambrian tectonics in the amalgamation of East and West Gondwana [1–6]. In several cases, rare-element mineralizations in the Egyptian Eastern Desert are confined to shear zones characterized by wall-rock alteration zones, quartz veins, and stockworks with remarkable enrichment in primary and secondary ore minerals, e.g., [7–10].

U and Th mineralizations in Egypt are hosted by granitic rocks mostly and their associated pegmatites, but sometimes they are hosted by relatively younger alkaline volcanics such as bostonite dykes and trachyte plugs, e.g., [11–20]. The mineralizations are represented by noticeable enrichment in high-field-strength elements (HFSEs) such as U, Th, Zr, and Y, in addition to rare-earth elements (REEs) and rare metals such as Nb and Ta associated with alkaline A-type granites, mainly formed during the late Neoproterozoic post-collisional stage some 630–580 Ma ago, either as disseminations in host granite or hydrothermally altered granite inside the shear zones [21]. In a recent review, [22] assorted the U-Th-REEs resources in Egypt hosted in Phanerozoic rocks, i.e., younger than 543 Ma, as follows: (1) Mesozoic alkaline ring complexes, (2) Post-Cretaceous peralkaline ring complexes, (3) Carboniferous siliclastics, and (4) Neogene black sands either on the Mediterranean Sea or the Red Sea beaches.

In similar worldwide occurrences, radioactive and rare-metal minerals suffer from variable degrees of alteration due to the deformation and circulation of hydrothermal fluids, which can lead to a diversity of secondary minerals hosting U-Th-Nb-Ta-REEs [23–25]. This results in new mineral assemblages that witness alteration events characterized by fluctuation and variation in physicochemical conditions [26]. The main aim of our study is to present details of the petrography and mineralogy of highly deformed rocks in the Wadi Nugrus area, with the possible impacts of the so-called "Najd Shear System (NSS)". The present work represents a combination of in situ spot analyses, such as electron microprobe (EMPA) and energy-dispersive spectral (EDS) analyses, to obtain the chemical details of secondary minerals and their relationship with the alteration processes. The aim is to propose a paragenetic sequence for the different stages of crystallization of ore minerals. Also, details of the scenario for the genesis of secondary ore minerals in terms of structure destabilization and the conversion of mineral phases through deformation and alteration are proposed. This destabilization includes the alterations of some accessory minerals such as zircon and apatite. These two minerals help trace hydrothermal alterations and sometimes act as mineralization indicators because of chemical variations when the mineral breaks down, e.g., [20,22,26–29]. Hydrothermal alterations of magmatic apatite, together with interstitial fluorite, result in the re-distribution of REEs; Y, Ca, P, and F as recorders of hydrothermal fluid chemistry; and physicochemical conditions and proportions of light components, e.g., F: Cl: OH [30,31].

2. Geological Setting

The boundary between the Central Eastern Desert (CED) and the Southern Eastern Desert (SED) was defined in [32]. It is based on the differences in rock associations and major structures developed during the East African orogeny (EAO) as part of the Pan-African orogeny during the Neoproterozoic. Later, several workers, e.g., [1,2,5,6,33–36], agreed with this distinction but proposed different hypotheses to explain tectonic evolution. Thus, there were disputes about whether there were infrastructural or pre-Pan African rocks. For such a reason, [37] stressed separating the CED from the SED using a thick zone of shear foliated rocks in the Migif-Hafafit and Wadi Nugrus areas extending to the Red Sea coast in a major NW-SE shear zone, as shown in Figure 1. This figure shows more than one major NW-trending thrust separating the gneisses from the ophiolites and arc-related assemblages in (1) Wadi Nugrus, (2) Wadi Ghadir, (3) Gabal Sikait, and (4) Gabal Zabara. In the present research, authors deal with deformed rocks, in a shear sense, at the Wadi Nugrus area where A-type granite is emplaced and sheared along the NW-SE Sha'it-Nugrus Shear Zone (SNSZ) (Figures 1 and 2). In the Wadi Nugrus area (Figure 2), rock types are represented by dismembered ophiolite, its mélange, gneissose granitoids, and granites. The A-type granites in the area are distinguished into biotite granite (mostly monzogranite) and leucogranite (syenogranite and alkali feldspar granite). These A-type granites show distinct marks of deformation owing to the SNSZ, which started some 600 Ma ago during the extensional phase in the Nubian Shield, i.e., syn-kinematic intrusions that followed the ~680 Ma arc collision and NW-trending thrust nappes [6,36–38].

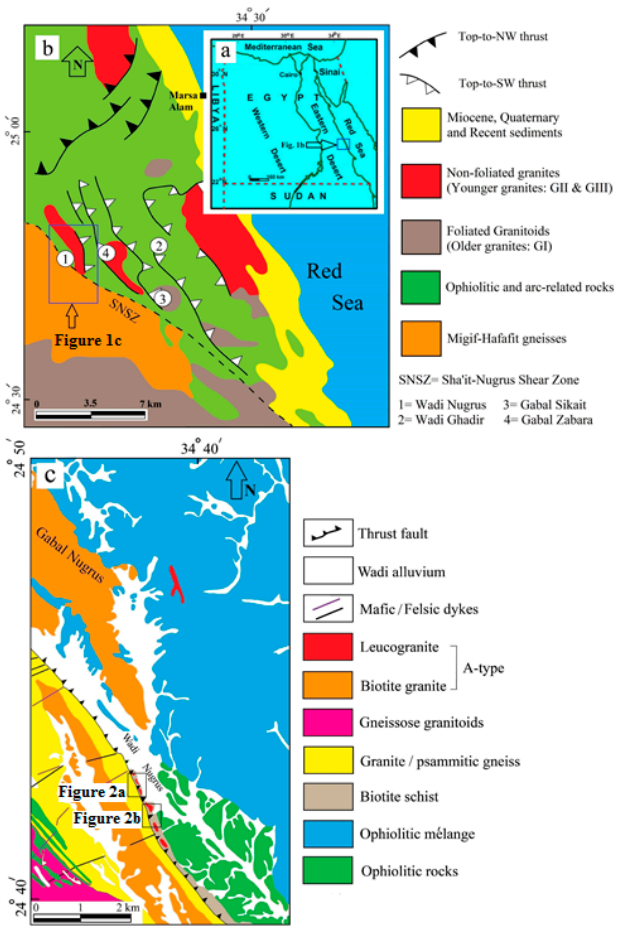

Figure 1. (**a**) Location map of the study area. (**b**) Geological map of the El Gemal-Hafafit district showing the major lithologies and structures. The NW-trending Sha'it-Nugrus shear zone (SNSZ) is shown as well as major thrusts (after [39]), and (**c**) a detailed geological map of the Wadi Nugrus area modified after [34].

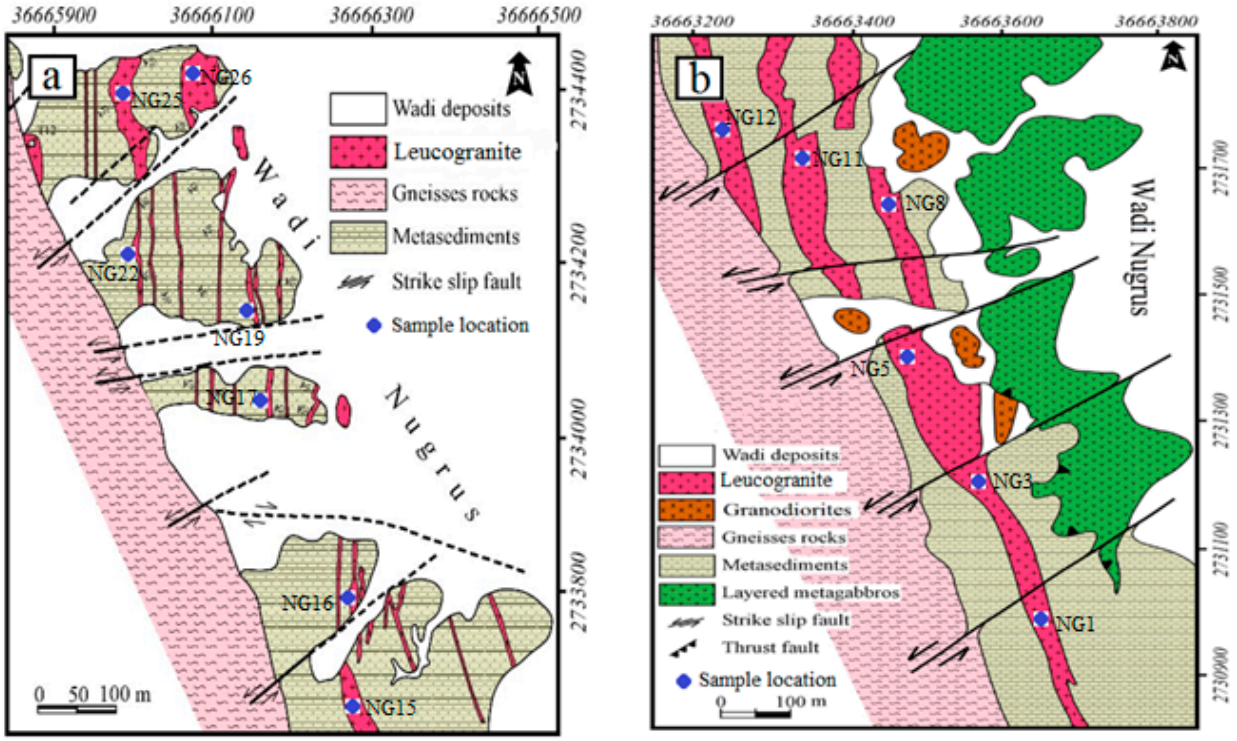

Figure 2. (**a**,**b**) Detailed maps for two localities showing the alignment of the investigated leucogranite (mineralized A-type granite) with respect to other rock units in the shear zone and along the Nugrus thrust [40]. The exact locations of the detailed maps are shown in Figure 1c.

Wadi Nugrus is a major tributary of Wadi El-Gemal, where a pile of Neoproterozoic rocks belonging to the ANS crop out. In the western part of the Wadi El-Gemal area, mineralized rocks are present, and they are hosted by different rock lithologies such as gneisses, granites, pegmatites, and dykes, e.g., lamprophyre dykes. From a geotectonic point of view, the west Wadi El-Gemal area, which includes Wadi Nugrus, represents the eastern extension of the highly deformed Migif-Hafafit gneissic belt. Generally, the Neoproterozoic rocks comprise metamorphic rocks (gneisses and migmatites), ophiolitic rocks, metasediments, arc metagbbro, older granitoids, younger granites, pegmatites, and aplites. Some workers believed the gneisses and migmatites were infrastructural rocks [35,41,42]. This infrastructure (mostly gneisses) is older than the ophiolitic mélange and intrusive rocks. It may represent an old continental crust before sea-floor spreading, metamorphism, and the development of the ophiolitic rocks. The area is highly tectonized and subjected to multi-episode folding during the compressional phase of the Pan-African orogeny [34]. In the Wadi Nugrus area, there are several thrusts and shear zones, which mostly follow an NW-SE trend. The Nugrus leucogranite occurs as scattered stocks, which are typically A-type, post-collisional, and show evidence of NW-trending deformation caused by the so-called "Najd Shear System (NSS)" in the western Arabian–Nubian Shield [43,44].

3. Field Observations

Field observations document the occurrence of gneisses that might be older than the ophiolitic mélange, e.g., the mineralized psammitic gneiss at Wadi Abu Rusheid and its counterparts in the Migif and Nugrus areas. Two types of metasediments are distinguished. The melange matrix for the ophiolitic fragments (serpentinite, talc-carbonate, metagabbro, and metadiabase) represents the first type. The second type is arc-related metasediments, represented by metamorphosed volcano sediments overriding the ophiolitic rocks along thrust faults. According to [45], the area was influenced by medium- to high-pressure

metamorphism (5–7 kb) as indicated by the mineral chemistry of garnet amphibolite, which is conformable to the metasediments. The Wadi Nugrus area has very characteristic A-type granite exposures aligned along the NW-trending Nugrus thrust and shear zone, as shown in the geological map (Figure 1).

Within the Nugrus shear zone (Figure 2), a conspicuous mass of leucogranite (monzogranite) trending NNW-SSE intrudes into the arc-related rocks. This granite mass is intensively sheared and belongs to the GII or A-type younger granites of Egypt (610–590 Ma) [43] and occurs as elongated monzogranite that extends for a length up to 4.5 km and is 150–500 m wide. The mass is highly jointed (Figure 2a) and is dissected by NNW-SSE strike-slip faults, which causes the occasional dislocation of the leucogranite and the associated aplite and pegmatite dykes [43]. There are three sets of joints trending: N-S, NNE-SSW, and NW-SE. In some instances, there are xenoliths of older rocks, particularly the arc-related biotite schist, in the leucogranite. This leucogranite is highly jointed andsheared (Figure 3), and the width of the shear zone is variable (0.5 m to >20 m) with the darkening of sheared granite owing to the circulation of metal-rich hydrothermal fluids. At several exposures, the most distinct alteration is argillic and, to a much lesser extent, ferruginous and carbonaceous. Occasionally, the granite is traversed by NW-SE fresh mafic dykes (Figure 3c) and non-mineralized/barren quartz veins that trend N 35–50° E.

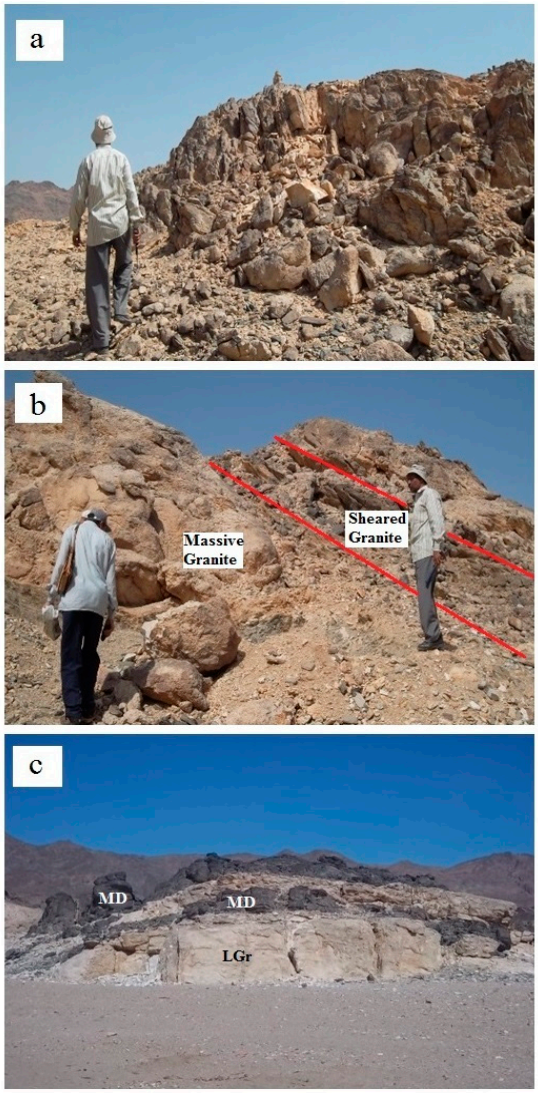

Figure 3. (**a**) Jointing in massive leucogranite, (**b**) shearing of the leucogranite, and (**c**) mafic dykes (MD) traversing the leucogranite (LGr).

4. Methods

Sampling was performed during two successive field trips to the Wadi Nugrus area. Systematically, the samples range from massive to deformed leucogranite outside and inside the NSZ. For the petrographic study, thin and polished sections were prepared and examined in both transmitted and reflected light. To obtain spectral analysis before the electron microprobe measurements, a scanning electron microscope model Prisma E SEM equipped with an energy dispersive X-ray spectrometer (EDS) for spot analysis of minerals was used. It is housed in the Nuclear Materials Authority of Egypt (NMA) laboratories in Qattamiya, Cairo. The analytical conditions were 25–30 kV accelerating voltages, 1–3 nm beam resolution, and 60–120 s counting time. Some back-scattered electron (BSE) images were taken by the SEM facility and electron microprobe. Mineral chemical analyses were obtained from four polished thin sections, which were analyzed using a JEOL jxa8900 electron microprobe manufactured in Japan, and housed at the University of Nevada, Las Vegas, USA. The polished thin sections were coated with ~15 nm of amorphous carbon to make them conductive during the vacuum coater-assisted preparation process for microprobe studies. The operating parameters included a 15 kV accelerating voltage, 10 nA beam current, 5–10 μm beam diameter, and 30-s count time on peak. Synthetic and natural mineral standards and the CITZAF matrix correction process were used for calibration.Excel sheets (self-made spreadsheets in Microsoft Excel) were used to calculate structural formulae of the analysed minerals.

5. Petrography and Ore Mineralogy

The leucogranite consists of K-feldspars, plagioclase, quartz, and mica. To a lesser extent, the K-feldspars are represented by homogeneous microcline, orthoclase, or microcline perthite. The latter is mostly vein, braided, and string perthite types, which are corroded by quartz (Figure 4a). This figure also shows the occurrence of mica flakes, either biotite or muscovite. The investigated granites, either fresh or hydrothermally altered, are characterized by a high modality content of accessory minerals in the 1.5 to 6% range. Fresh, i.e., unaltered granites contain disseminated zircon and columbite. Zircon is coarse and may reach up to 350 μm in its cross-sectional cut perpendicular to the C-axis (Figure 4b). Other accessory minerals include rare metals, mostly columbite and its alteration phases (Figure 4c), and thorite. It is common to observe radioactive haloes around fergusonite in coarse biotite flakes as one of the columbite alterations (Figure 4d).

First, opaque minerals were identified by a reflected light microscope as far as the authors found possible. Then, the ore microscopic investigation was confirmed and enhanced using back-scattered electron images (BSE) taken during the electron microprobe and the SEM-EDS microanalysis. Figure 5 shows the collective assembly of ore minerals in the BSE images of the electron microprobe. Primary ore minerals are mostly represented by zircon, columbite, and much lesser thorite, which show variable degrees of freshness and homogeneity. The size of zircon exceeds that of columbite and takes it as inclusions occasionally, in addition to fresh columbite adjacent to zircon (Figure 5a). Figure 5b shows two domains in the same columbite crystals where thorite inclusions are still preserved in the fresh domain.

In contrast, the altered domain lacks thorite and is represented by an intergrowth of hydrothermal minerals (fergusonite and hydropetscheckite). In some instances, the alteration of columbite is represented by fergusonite only (Figure 5c). Fergusonite appears as cracked crystals with the crust of an unidentified mineral halo due to metamictization (Figure 5d). The intergrowth of fergusonite and petscheckite is seen without any columbite relics when the latter is completely altered (Figure 5e). The intergrowth of hydrothermal minerals (Nb-bearing minerals “niobates”) replacing columbite can be formed from

fergusonite–petscheckite–uranopyrochlore (Figure 5f). Thorite does not occur as minute inclusions in columbite only but in the form of about 100 µm wide independent crystals, which are severely altered (Figure 5g). In fresh magmatic columbite, silicate inclusions are encountered alongside thorite (Figure 5h). Accessory minerals with no or negligible alteration are present in the fresh and deformed granite with the lowest alteration imprints. In contrast, fluorite and apatite are completely altered in the highly altered and deformed granite samples. In this case, the anions and cations of these two accessory minerals are re-distributed among the newly formed hydrothermal phases in the investigated granite, presented in the Mineral Chemistry Section and Discussion.

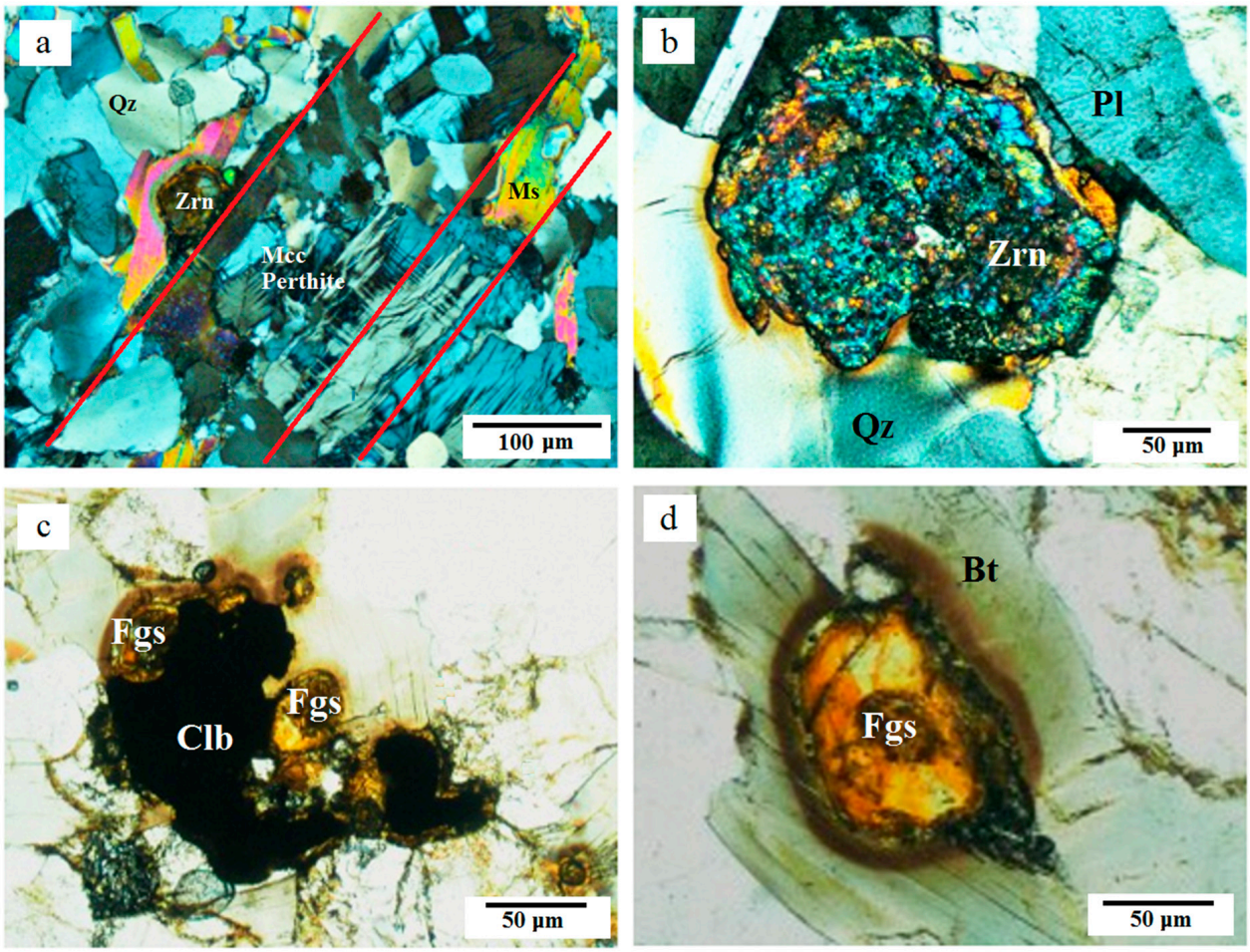

Figure 4. Photomicrographs of the sheared Nugrus leucogranite. (**a**) Shearing, defined by parallel red lines, in the leucogranite consisting of microcline (Mcc) perthite, quartz (Qz), plagioclase (Pl), muscovite (Ms), and zircon (Zrn), CN; (**b**) close-up view of coarse euhedral zircon (Zrn) in groundmass made up of quartz (Qz) and plagioclase (Pl), CN; (**c**) columbite (Clb) partly altered to fergusonite (Fgs), PPL; and (**d**) details of pleochroic haloes of fergusonite (Fgs) in biotite (Bt), PPL. CN = crossed-nicols and PPL = plane polarized light. The mineral abbreviations are recommended by the IMA [46].

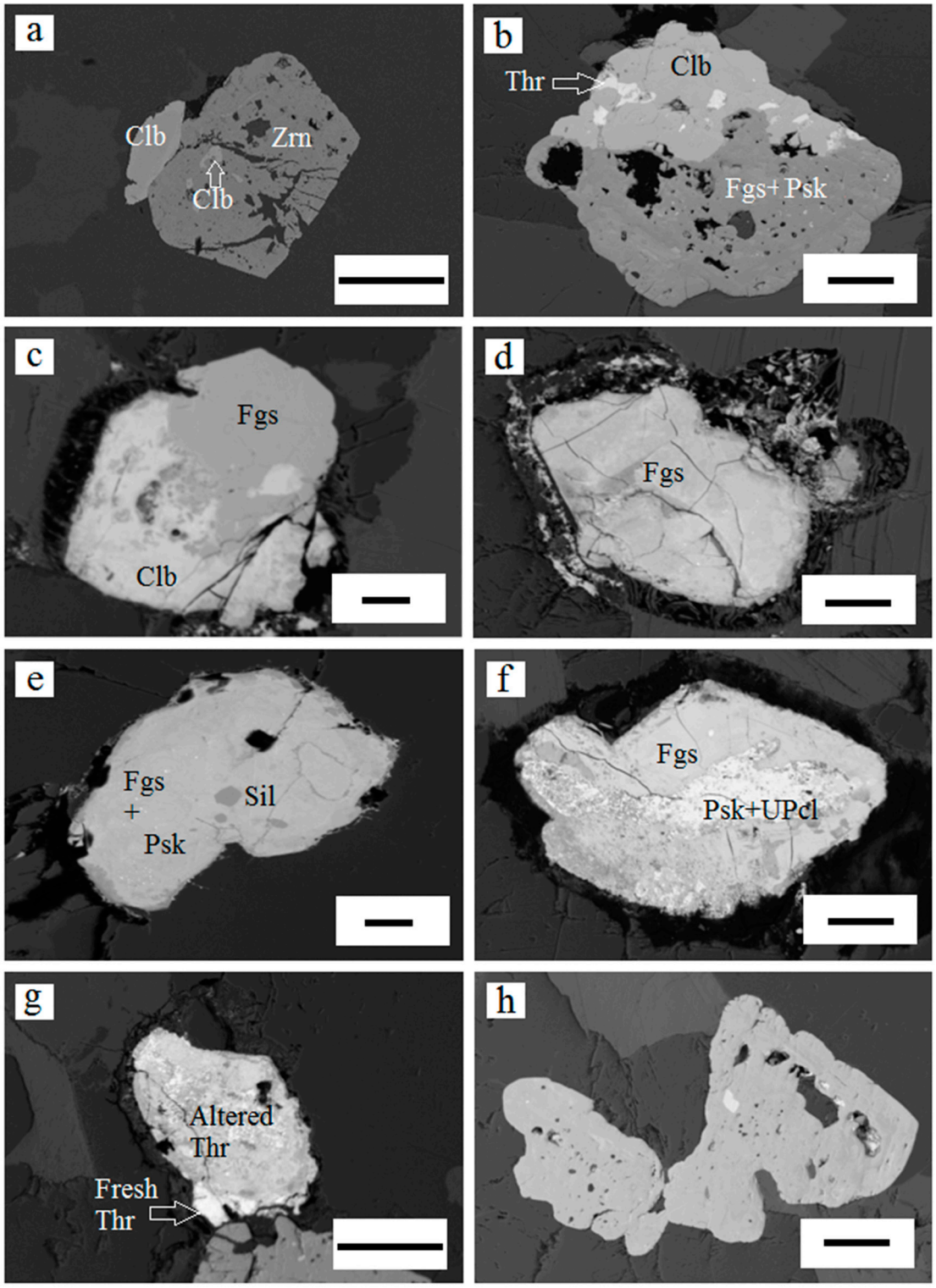

Figure 5. BSE images captured by the electron microprobe. The bar scale for all equals 50 µm. (**a**) Magmatic columbite (Clb) is juxtaposed and enclosed by coarser euhedral zircon (Zrn). The latter shows idiomorphism same as in Figure 4b. (**b**) Columbite, with thorite inclusions (Thr), extensively altered to fergusonite (Fgs) and petscheckite (Psk) along a replacement contact. (**c**) Irregular partial replacement of columbite (Clb) to fergusonite (Fgs). (**d**) Homogeneous fergusonite (Fgs) with a metamict halo. (**e**) Fergusonite petscheckite (Psk) alteration, pseudomorphing ferrocolumbite, enclosing sub-rounded silicate inclusions (Sil). (**f**) Fergusonite with patchy alteration to a mixture of petscheckite (Psk) and uranopyrochlore (UPcl). (**g**) Extensively altered subhedral thorite (Thr), and (**h**) coarse subhedral, i.e., sub-idiomorphic, with inclusions of silicate and bright rare metal-bearing mineral.

6. Mineral Chemistry

6.1. SEM-EDX Semi-Quantitative/Qualitative Microanalytical Data

Figures 6–8 provide the spectra of the investigated magmatic dissemination, and hydrothermal and supergene ore minerals. The preliminary investigation of the fresh columbite crystals by the EDX attachment revealed its characteristic iron peak; therefore, it is typical ferrocolumbite (Figure 6a). The spectrum of fresh ferrocolumbite indicates it is uraniferous and has some contents of yttrium (Figure 6b), which the EMPA confirms, as will be given in the following subsection. Upon the alteration of ferrocolumbite, fergusonite-Y forms with noticeable contents of rare-earth elements (REEs), namely Dy, Er, and Yb (Figure 6c). Some supergene minerals, which were not identified microscopically, are confirmed by the SEM-EDX spectra, such as altered uranothorite (Figure 7a). Two varieties of uranothorite are distinguished; both bear light and heavy REEs (La, Nd, Ce, Pr, Sm, Eu, and Gd), and one is P-F-rich (Figure 7b). Altered betafite occurs as a complete pseudomorph after columbite (Figure 7c). This betafite is uraniferous and bears appreciable content in REEs and Y. About 95% of the sulfide minerals are represented by pyrite, commonly altered to Fe-oxyhydroxides (Figure 8a). The sulfide percentage comprises galena and sphalerite (Figures 8b and 8c, respectively). Owing to the sulfides' tiny size, some Si and Cl peaks from the silicate background appear.

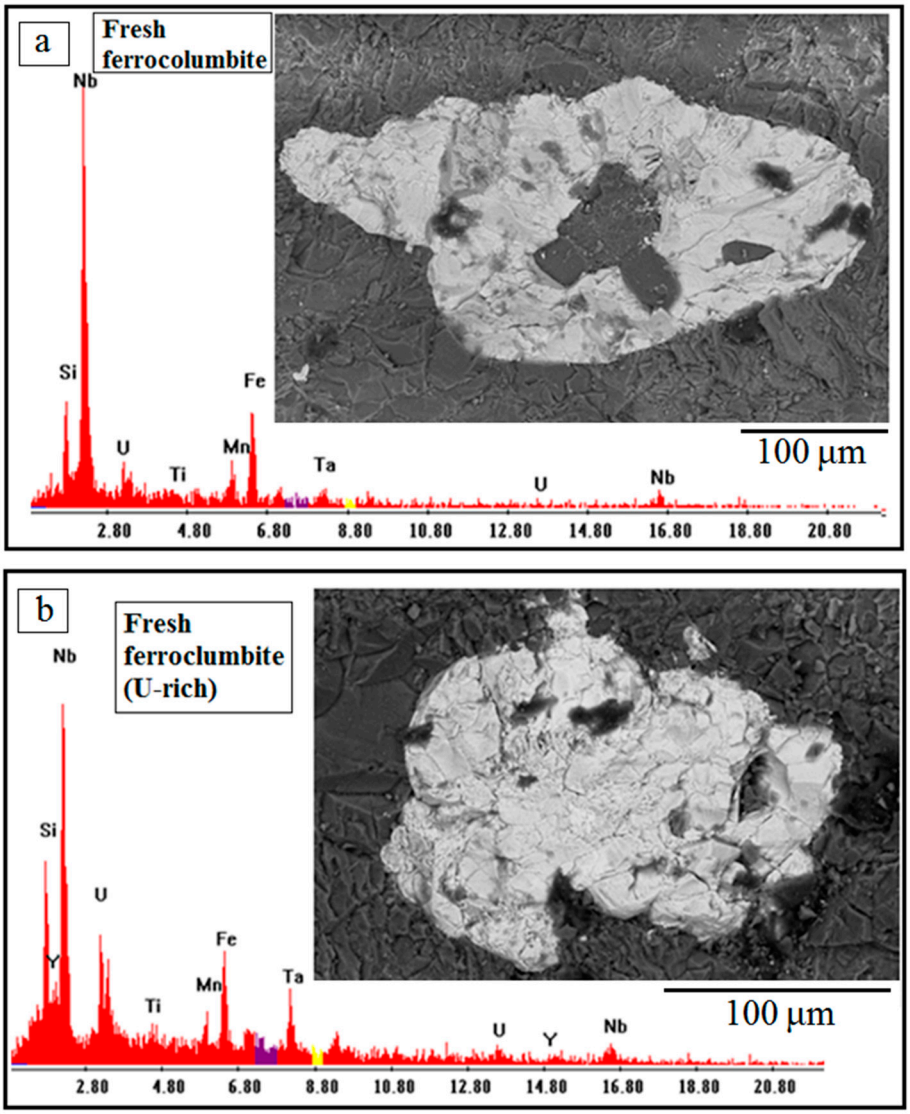

Figure 6. *Cont.*

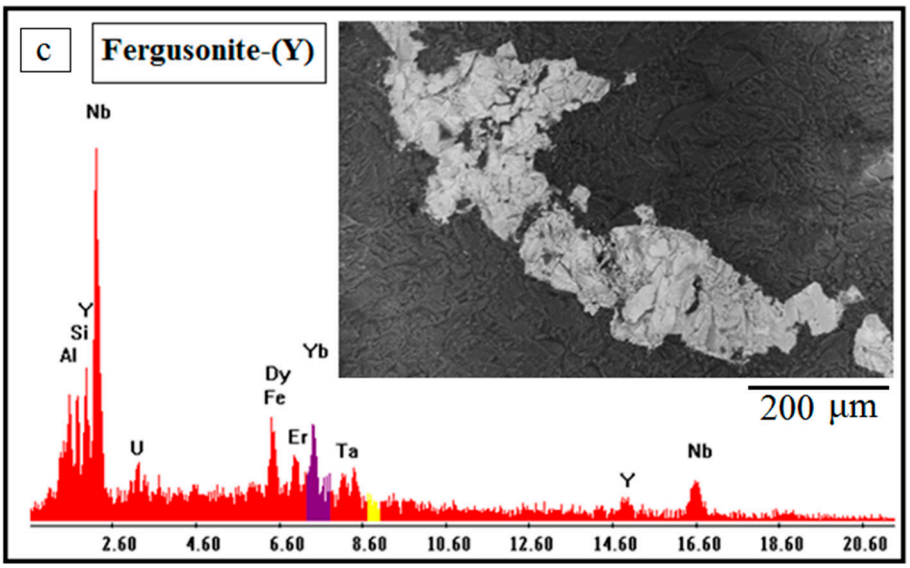

Figure 6. Spectral analyses and BSE images captured by the scanning electron microscope. (**a**) Fresh ferrocolumbite, (**b**) U-rich fresh ferrocolumbite, and (**c**) fergusonite-Y.

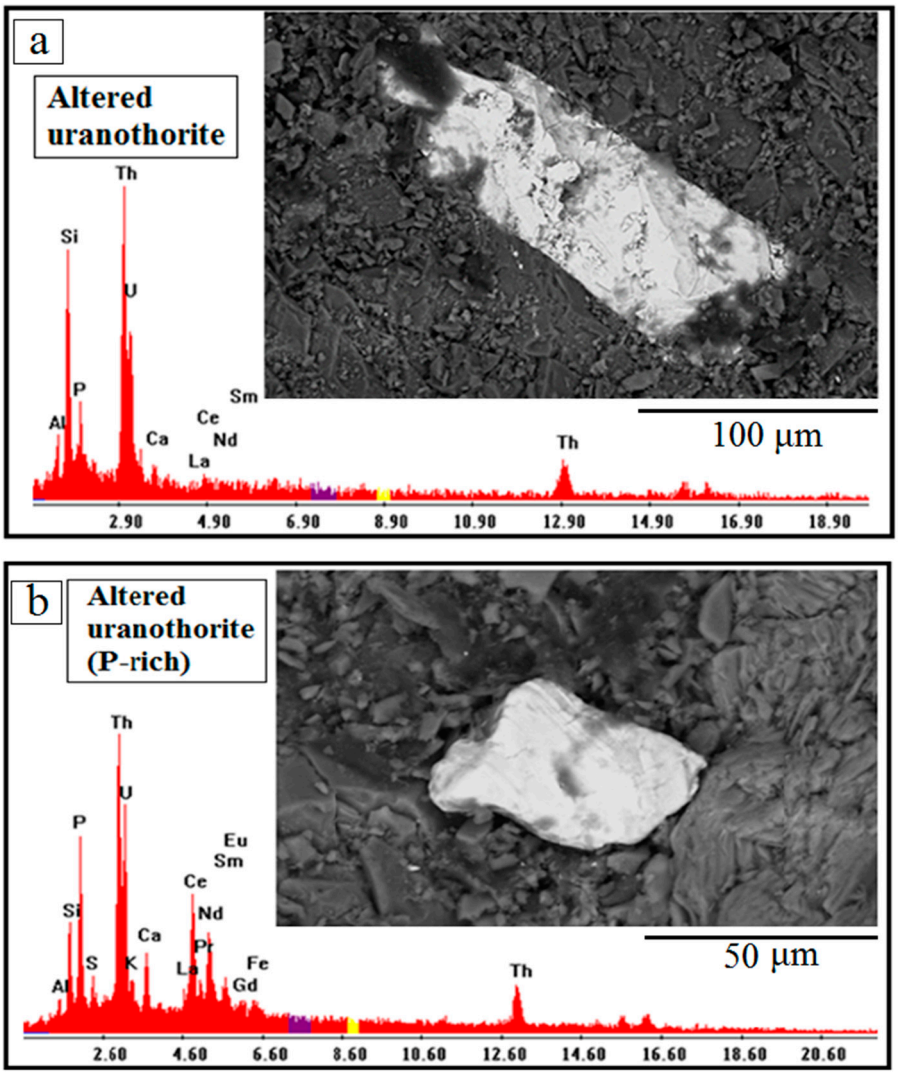

Figure 7. *Cont.*

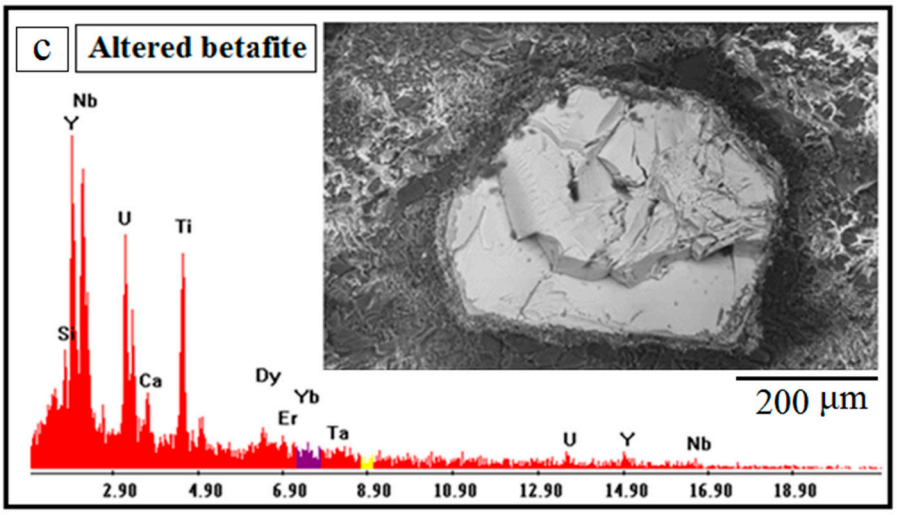

Figure 7. Spectral analyses and BSE images captured by the scanning electron microscope. (**a**) Altered uranothorite, (**b**) P-rich altered uranothorite, and (**c**) altered betafite.

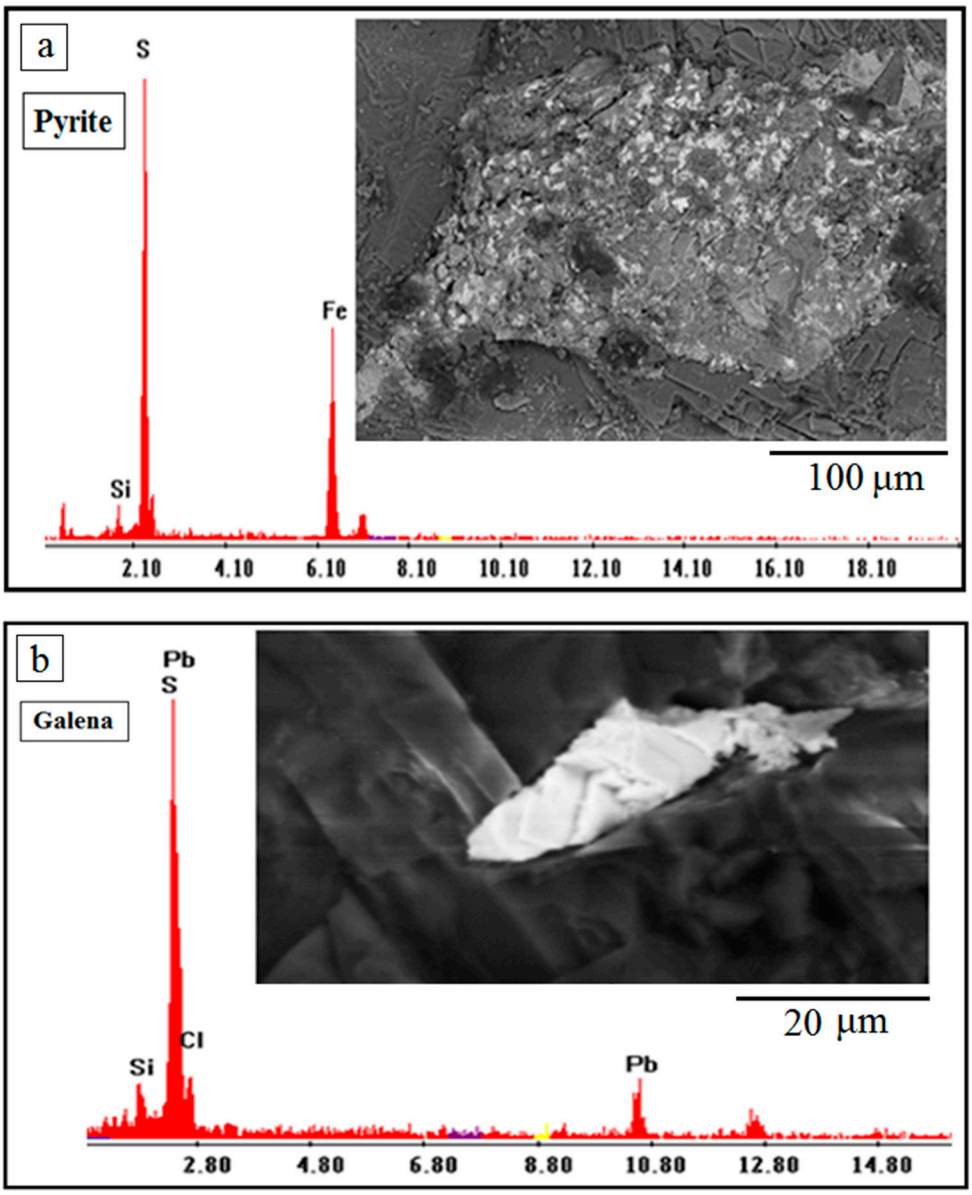

Figure 8. *Cont.*

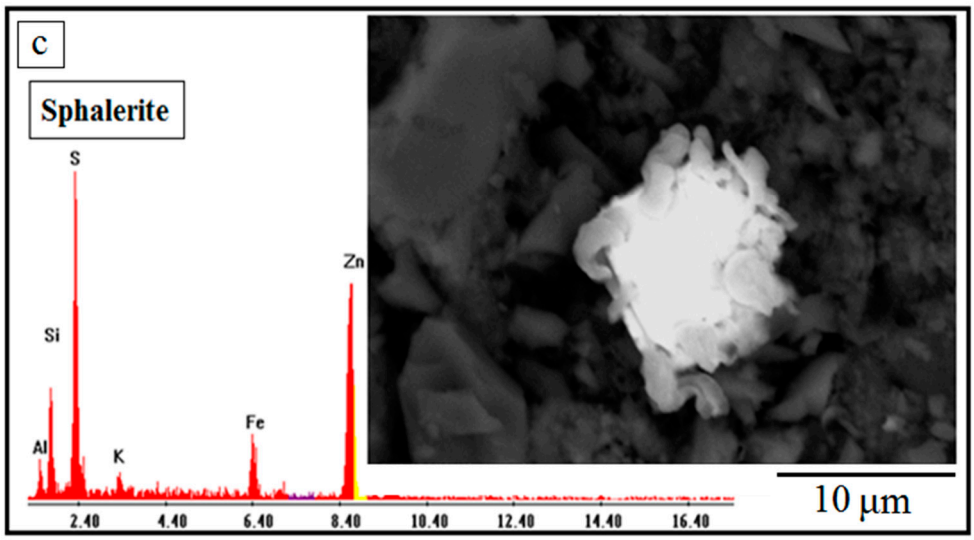

Figure 8. Spectral analyses and BSE images of sulfides captured by the scanning electron microscope. (a) Pyrite, (**b**) galena, and (**c**) sphalerite.

6.2. EMPA Quantitative Microanalysis

The electron microprobe analysis (EMPA) results are obtained for all the ore minerals, either primary (magmatic and hydrothermal) or secondary supergene (Supplementary Table S1a–g). Tables 1–3 are extracted from the bulk microprobe data to characterize these ore minerals' chemical composition numerically.

Table 1. Summary of the rare-element minerals in the deformed Nugrus A-type granite.

	Mineral	Mineral Variety 1	Mineral Variety 2	Mineral Variety 3
(1)	Columbite (ferroan)	Fresh (18 analyses)	Slightly altered (1 analysis) 95.56 wt% Sum 3.23 wt% P_2O_5 3.75 wt% Ce_2O_3	-
(2)	U- and Th-bearing Nb-Ta minerals	Fergusonite-(Y) (25 analyses)	Petscheckite (3 analyses)	Uranopyrochlore (3 analyses)
(3)	F- and P-bearing thorite	Stage I Ce-bearing thorite/thorianite	Stage II Ce-bearing thorite	Stage III U-Nb-Y-bearing thorite
(4)	Zircon	Fresh (7 analyses)	-	-
(5)	Altered uranothorite	-	-	-
(6)	Altered betafite	-	-	-

Table 2. Compositional ranges of destabilized columbite (U- and Th-bearing niobates).

Oxide Range wt%	Mineral		
	Fergusonite-(Y)	**Petscheckite**	**Uranopyrochlore**
Nb_2O_5	38.03–47.94	43.63–46.85	38.99–40.6
Ta_2O_5	5.78–8.15	7.13–10	7.16–10.57
UO_2	9.08–15.24	1.26–7.86	6.59–10.88
ThO_2	3.33–7.13	3.48–5.71	5.4–9.52
ZrO_2	0–0.15	0.18–1.18	0.41–1.05
Y_2O_3	3.79–6.03	0.31–2.93	1.37–2.65
SiO_2	0.86–1.96	4.57–11.22	4.41–9.86
Total (anhydrous)	77.02–86.22	82.18–87.2	75.34–86.22

Table 3. Chemical characteristics and compositional ranges of major components in the F-P-bearing thorite phases.

Mineral	**Ce-Bearing Thorite/Thorianite**	**Ce-Bearing Thorite**	**U-Nb-Y-Bearing Thorite**
Stage	I	II	III
Degree of destabilization	Lowest	Moderate	High
Th	Highest ThO_2 content (50.16–60.12 wt%)	Moderate ThO_2 content (41.38–45.13 wt%)	Lowest ThO_2 content (22.58–23.63 wt%)
P	P_2O_5-rich (13.7–15.6 wt%)	P_2O_5-rich (15.95–17 wt%)	P_2O_5-poor (6.34–9.14 wt%)
F	F-rich (2.73–5.61 wt%)	F-rich (3.3–4.11 wt%)	F-poor (1.55–2.07 wt%)
Y	Y_2O_3-poor (0.38–0.95 wt%)	Y_2O_3-poor (0.7–0.83 wt%)	Y_2O_3-rich (0.38–0.95 wt%)
Nb	Nb_2O_5-poor (0.18–1.41 wt%)	Nb_2O_5-poor (0.3–1.22 wt%)	Nb_2O_5-rich (3.28–7.92 wt%)
U	Lowest UO_2 content (0.47–0.95 wt%)	Lowest UO_2 content (0.64–0.65 wt%)	Slightly uraniferous (1.66–1.69 wt% UO_2)
S	SO_3-rich (1.31–2.34 wt%)	SO_3-rich (1.42–2.20 wt%)	SO_3-poor (0.24–0.26 wt%)
Zr	Low (1–2.52 wt%)	Intermediate (2.29–3.45 wt%)	High (7.75–13.75 wt%)
Ca	CaO-rich (3.73–5 wt%)	Intermediate CaO content (3.12–3.49 wt%)	CaO-poor (1.3–1.37 wt%)
SiO_2	SiO_2-poor (2.4–5.22 wt%)	SiO_2-poor (3.78–4.03 wt%)	SiO_2-rich (14.56–18.79 wt%)
Na_2O	Sodic (1.33–2.28 wt% Na_2O)	Sodic (1.51–1.8 wt% Na_2O)	Na_2O-poor (0.06–0.07 wt%)

The analyses of columbite (Supplementary Table S1a) confirm its ferrous variety in which FeO ranges from 14.63 to 16.39 wt%, whereas the content of MnO is almost a third (4.3–5.44 wt%). Nb_2O_5 in this fresh ferrocolumbite ranges from 62.43 to 70.95 wt%. Ferrocolumbite with the lowest Nb content bears the maximum Ta_2O_5 content (15.91 wt%), and this is a normal cationic substitution of Nb and Ta in the columbite–tantalite series. All

the spot analyses of ferrocolumbite show content of Y_2O_3 in the range of 0.33–0.45 wt%. Some ferrocolumbite crystals have ThO_2 and UO_2 contents up to 0.87 wt% and 0.38 wt%. The contents of F, SO_3^-, and the oxides of Hf and Ce are very minor. On the other hand, the concentrations of these elements in the hydrothermal alteration products of ferrocolumbite (Supplementary Table S1b,c) are different. Table 1 provides the compositional ranges in these secondary niobates. They show very distinct leaching of Nb_2O_5, which lies in the ranges 38.03–47.94 (fergusonite-Y), 43.63–46.85 wt% (petscheckite), and 38.99–40.60 wt% (uranopyrochlore). Ta_2O_5 follows the same trend of leaching, which amounts to 5.78–8.15 wt%, 7.13–10 wt%, and 7.16–10.57 wt% in the three hydrothermal niobates, respectively. The lowest leaching of FeO is noticed in petscheckite (7.88–9.24 wt%) but noteworthy to report a wide range of FeO content (2.48–11.92 wt%) in the fergusonite-Y. The contents of UO_2, ThO_2, and Y_2O_3 are noticeably high. In these niobates, UO_2 reaches up to 15.24 wt%, 7.86 wt%, and 10.88 wt% in ferugsonite-Y, petscheckite, and uranopyrochlore, respectively. Similarly, ThO_2 (up to 7.13 wt%, 5.71 wt%, and 9.52 wt%, respectively). In comparison with their nearly Y-free magmatic precursor (ferrocolumbite), these three niobates contain appreciable Y_2O_3 in the ranges 3.79–6.03 wt%, 0.31–2.93 wt%, and 1.37–2.65 wt%, respectively. The oxides percentage of the three niobates never exceeds ~87 wt%. On the other hand, the sum of oxides in the columbite precursor is ideally 100%, which indicates that the sum of oxides in the columbite precursor is ideally 100%, which indicates the ultimate degree of freshness. The chemistry of the analyzed fergusonite-Y, for example, is not similar to that of the primary fergusonite in nature. Therefore, our Nugrus fergusonite is somehow destabilized and compositionally similar to another hydrothermal niobate, namely liandratite [U^{6+}(Nb, Ta)$_2O_8$]. A minor amount of a fourth hydrothermal niobate (altered betafite) is developed at the expense of the magmatic dissemination of ferrocolumbite in the Nugrus deformed leucogranite (Supplementary Table S1a). It shows leached Nb_2O_5 and Ta_2O_5 contents (20.23 wt% and 5.66 wt%, respectively). TiO_2 content (20.55 wt%) is typical of betafite with appreciable amounts of UO_2 and Ce_2O_3 (3.46 wt% and 8.53 wt%, respectively). Sometimes, destabilized fergusonite-Y is found as a homogeneous phase without any other niobate phase. In this case, the fergusonite is typically uraniferous and with UO_2 content in the range of 8.44–15 wt% whereas the range is 2.59–7.13 wt% for ThO_2 and 3.79–6.17 wt% for Y_2O_3.

Another group of destabilized or hydrothermal minerals is thorite, with peculiar contents of fluorine and phosphorous (Table 3 and Supplementary Table S1d). As can be seen in the summary of composition and ranges of oxides (Table 3), these destabilized Th-bearing minerals do not pertain to the typical chemistry of magmatic thorite. Based on color in the BSE images, three F- and P-bearing destabilized thorite can be distinguished, representing three successive stages of hydrothermal alteration, namely stages I (Ce-bearing thorite), II (another phase of Ce-bearing thorite), and III (U-Nb-Y-bearing thorite). Ce-bearing thorite of stage I is sodic (1.33–2.28 wt% Na_2O) and relatively poor in SiO_2 (2.4–5.22 wt%). Stage I Ce-bearing thorite is rich in CaO (3.73–5 wt%), P_2O_5 (13.7–15.6 wt%), SO_3^- (1.31–2.34 wt%), and F (2.73–5.61 wt%). The chemical composition of stage II Ce-bearing thorite indicates a similar sodic nature (1.51–1.8 wt%) and relative enrichment in P_2O_5 (15.95–17 wt%). On the other hand, stage III U-Nb-Y-bearing thorite is not sodic (0.06–0.07 wt% Na_2O) and contains the highest silica content among the whole destabilized phases (14.56–18.79 wt%) and the highest ZrO_2 (13.75 wt%) as well. Compared to the Ce-bearing thorite, the U-Nb-Y-bearing thorite is poorer in P_2O_5 (6.34–9.14 wt%), F (1.55–2.07 wt%), and CaO (1.3–1.37 wt%). A single analysis of destabilized thorite (39.08 wt% ThO_2 and Σ oxides = 83.52 wt%) is presented in Supplementary Table S1e. It contains ~10 wt% UO_2, which can be considered uranothorite. Also, it is Zr-bearing

(6.14 wt% ZrO_2) and with 1.1 wt% F. Zircon is the lowest destabilized mineral, and its chemical composition (Supplementary Table S1f) is typical of magmatic nature.

EMPA of fresh pyrite is presented in Supplementary Table S1g). The contents of F and S are typical with the ratio 1:2, and the Σ Fe + S is almost 99.5 wt%. The ten analyses show that this pyrite is almost free of Ni and As (up to 0.02 wt% and 0.01 wt%, respectively). Considerable traces of Co and Cu are present (0.04–11 wt% and 0.04–0.15 wt%, respectively). The highest content of trace elements is represented by Pb (0.74–2.01 wt%).

7. Discussion

7.1. Metallogenic Significance and Stages of Ore Minerals Crystallization

The ANS is a well-known metallogenic province of rare metal and radioelement mineralization. In recent years, voluminous masses of felsic rocks in Egypt and Saudi Arabia have been investigated for mineral resources of Nb, Ta, U, Th, Y, and REEs hosted by post-collisional A-type granites (e.g., [21,47,48]). Among these granites, the leucogranites in the Nugrus area, as well as other localities in the Eastern Desert of Egypt, are believed to be formed by the partial melting of thickened crust followed by emplacement contemporaneous with the reactivation of old thrust zones in the form of strike-slip or shear zones [49–52]. In a review of Nb-Ta-U-Th-REEs resources in the Eastern Desert of Egypt, [21] reported that highly fractionated A-type granites are specialized for rare metals and radioelements, which accompany beryl, cassiterite, and fluorite mineralizations in some instances. It was also concluded that such deposits are occasionally enriched in Zr, Y, and F, typical of A-type granites and related niobium–yttrium–fluorine (NYF) pegmatites in post-collisional regime [53–56]. Based on the mineral chemistry of ore minerals in the studied leucogranite from Wadi Nugrus area (Table 1 and the Supplementary Table S1), it is evident that they are enriched in Nb, P, Y and F. Accordingly, they are similar to international examples of mineralized A-type granite and NYF pegmatite [57] as well as some Egyptian examples from the Eastern Desert, e.g., [16,21,58–63].

Based on ore mineral identification, textural relationships, and microanalytical data given in the results section, it is possible to define different stages of ore mineral crystallization and the paragenetic sequence. Figure 9 provides the suggested paragenetic sequence. Also, it distinguishes between minerals in the two primary stages, namely magmatic and hydrothermal. The microanalytical data in the Supplementary Table S1a–g and BSE images (Figures 5–8) indicate that the magmatic stage witnessed the crystallization of zircon, thorite, ferrocolumbite (Figure 10a), and possibly some of the fergusonite. It is supposed here that the magmatic paragenesis of the magmatic stage might include primary phosphate minerals (apatite, monazite, and xenotime) that are completely destabilized during the hydrothermal alteration, furnishing a considerable amount of P that converts magmatic thorite into hydrothermal P-F-rich thorite (Figure 10b, Table 3). Zircon has a typical magmatic nature, as indicated by the ThO_2/UO_2 >0.1 (Figure 11a). A single odd analysis of zircon (Figure 11a) would suggest limited hydrothermal destabilization. Another support for the freshness of this magmatic zircon is confirmed by its Si/Zr ratio equal to 1.08–1.16 (Figure 11b). In the fresh and undeformed Nugrus leucogranite, sulfide minerals are rare or almost absent. Still, they are common in the deformed samples (Figure 8), indicating their hydrothermal origin and, accordingly, hydrothermal destabilization or rare-element minerals formed in a reducing condition. In brief, ore minerals in the hydrothermal stage are represented by sulfides (dominated by pyrite), P-F-rich thorite, fergusonite-Y, petscheckite, and uranopyrochlore. Altered uranothorite and betafite (Figure 7) are counted among the supergene mineral assemblage.

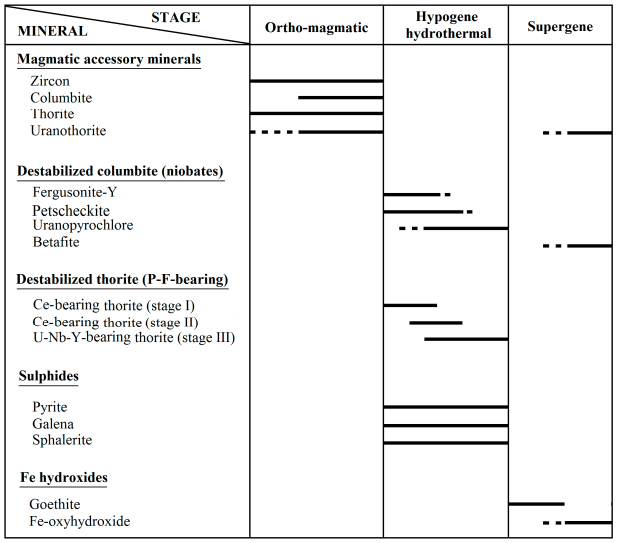

Figure 9. A proposed paragenetic sequence of ore minerals (rare metal and radioactive) in hydrothermally destabilized and deformed Nugrus leucogranite.

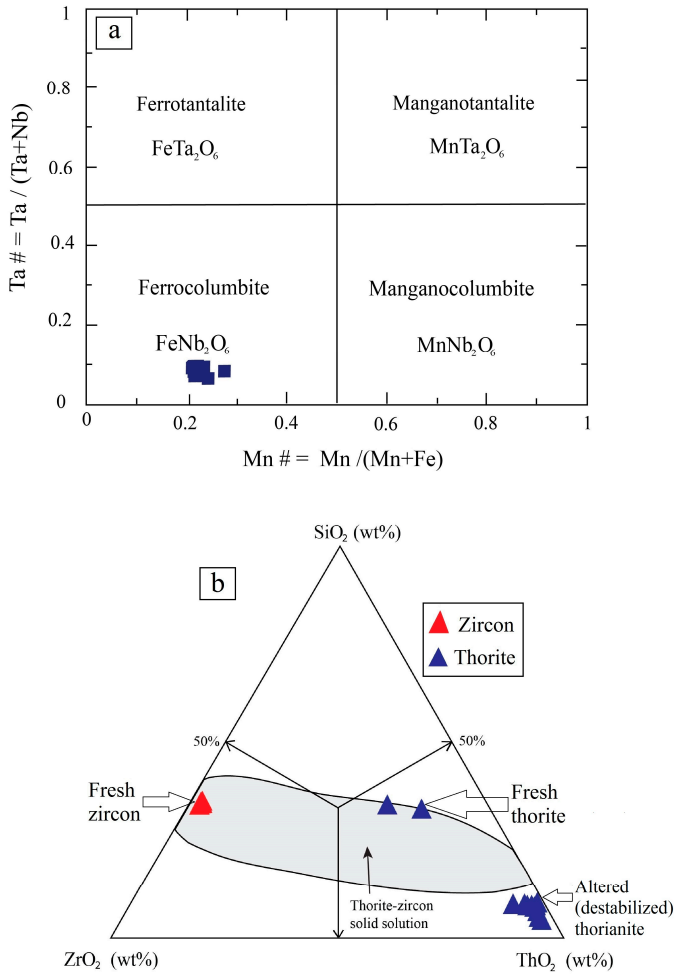

Figure 10. (**a**) The ferroan nature of columbite confirmed by the plots in the quadrilateral classification diagram after [64] adopted by [65], and (**b**) plots of analyzed zircon and thorite showing the freshness of zircon and some thorite, which are extensively altered due to hydrothermal destabilization. The field of the zircon–thorite solid solution is defined by [66,67].

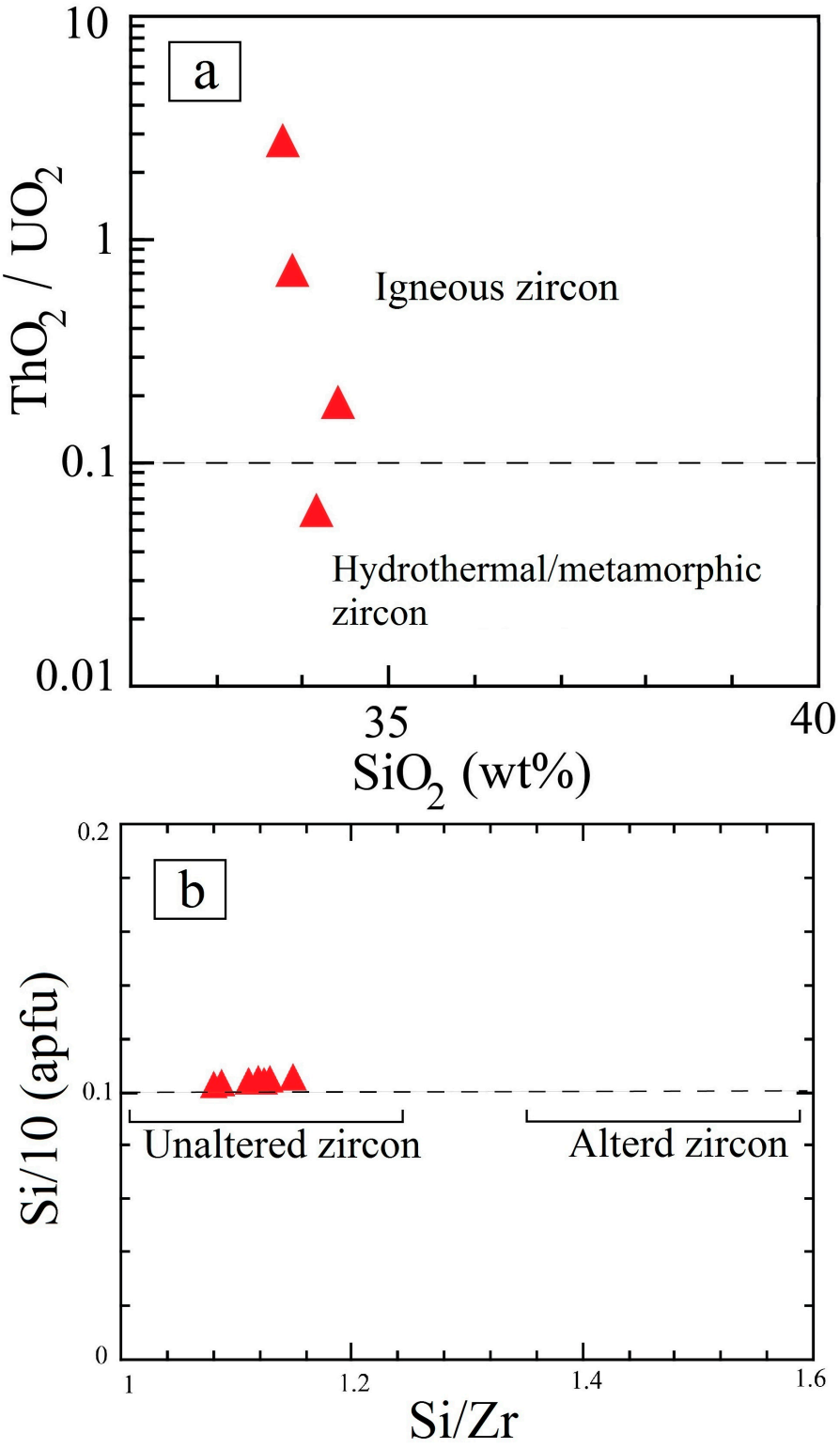

Figure 11. (**a**) Igneous nature of zircon based on discrimination recommended by [68], and (**b**) Si/Zr ratio < 1.2 indicating the freshness of zircon.

7.2. Mechanism of Ore Minerals Destabilization

During the hydrothermal stage(s) of mineralization, some essential elements play an important role in the crystallization of the A-type granite host. Fluxing elements and their enrichment are critical for crystallizing silicate and ore minerals in felsic magmas evolved in post-collisional settings, e.g., [69–71]. Therefore, the investigated rare-metal and radioactive minerals in the magmatic stage are believed to be concentrated in the highly fractionated

felsic melt once the rare elements are associated with considerable amounts of fluxing elements and compounds, e.g., F, P, and H_2O [69]. This is confirmed by the experimental work of [71], who agreed with [70,72,73] that these fluxing materials influence the concentration of rare elements and the viscosity and diffusivity of the residual hydrothermal fluid. In the case of the studied Nugrus leucogranite, this fluid becomes enriched in rare elements, including the radioelements, contemporaneous to elevated concentrations of P, Zr, and Th, which crystallize magmatic apatite, zircon, and thorite, respectively.

The textural criteria obtained from the BSE images in Figures 5 and 6 confirm such sequence and indicate that columbite crystallization is the latest among the primary dissemination of magmatic accessory minerals. Most likely, it crystallizes as the budget of iron reaches its ultimate level, as indicated by the ferroan nature of columbite (Supplementary Table S1a). The mineral is interstitial and post-dates rare-metal and radioactive minerals in fluorite samples. The crystallization of fluorite witnesses the transition from magmatic to hydrothermal once the solubility of H_2O increases. During the hydrothermal stage, F interacts with Ca-bearing country rocks. In this case, F is transported as fluoride complexes, and fluorite might form veinlets and veins after consuming rare elements in the magmatic stage [73–75].

In the Nugrus shear zone, the phosphate minerals, mainly apatite, broke down at the hydrothermal stage. Apatite-group minerals comprise hydroxyl-apatite (HAP), fluorapatite (FAP), and chlorfluor-apatite (CFA) [76,77]. The mechanism of phosphate breakdown is a dissolution process in hydrothermal conditions at pH = 2–7 and at low temperatures as low as 25 °C based on experimental mineralogy tests [78,79]. The crystallization of hydrothermal sulfides in the investigated Nugrus deformed granite enhanced apatite dissolution in the presence of Pb or Cd, as indicated by the presence of galena shown in Figure 8 [79]. Also, apatite dissolution in the Nugrus samples was enhanced by fluoride ions [80–82]. The liberated F and P are captured in the structure of newly formed F-P-bearing thorite and other rare-metal and radioactive minerals (Supplementary Table S1d). It is worth mentioning the destabilization includes magmatic ferrocolumbite and other magmatic accessories, e.g., U-Th minerals in the deformed Nugrus leucogranite (Figures 6 and 10a; Table 2 and Supplementary Table S1a), by hydrothermal solutions in the A-type granites. This corresponds to similar hydrothermal alteration in other localities in the Eastern Desert of Egypt, e.g., Gabal Gattar, El Erediya, and Um Ara localities [83–85]. Therefore, the present work agrees with these authors that rare element-bearing secondary minerals are the hydrothermal products of sheared A-type granite that manifest and accelerate by the argillic alteration and formation of clay minerals and Fe-oxyhydroxide. In the Nugrus case, magmatic U-Th minerals are replaced by supergene uranothorite and betafite (Figure 7, Supplementary Table S1e). On the other hand, ferrocolumbite is replaced by destabilized ferugosonite-Y, petscheckite, and uranopyrochlore (Figure 6; Supplementary Table S1b,c). In low-temperature hydrothermal conditions, OH-, H2O, and heat availability can replace the primary magmatic minerals with hydrothermal uranium niobate such as uranopyrochlore and petscheckite [86]. Experimental work by [87] indicates that petscheckite is a metamict mineral species. The latter authors give natural petscheckite with considerable REEs and U contents, similarly to the present study. In contrast to [88], magmatic columbite from the present Nugrus locality is a ferroan variety. Mn-columbite from some Egyptian pegmatites contains 13.5 wt% MnO on average [88]. Regardless of the end-members, either ferroan or mangoan, they crystallize by Fe-Mn fractionation followed by Nb-Ta fractionation. Magmatic zircon and thorite (i.e., primary) in the lowest deformed granite in the Nugrus shear zone are comparable to their counterparts from other world examples, e.g., Chinese [86]. In the present study, we confirm the conclusion by [89] that the fresh domains of zircon are low-(U + Th), whereas the composition of altered zircon

domains is high-(U + Th). Also, altered zircon shows a drastic drop in the contents of ZrO_2 and SiO_2 (up to 42 wt% and 23 wt%, respectively) [88]. We also agree that incorporating Ca, Fe, and Mg compensates for the loss in Zr and Si.

Based on the foregoing discussion, the proposed scheme of paragenetic sequence is presented in Figure 9, which distinguishes the primary stages into primary magmatic and hydrothermal sub-stages, and finally, a supergene stage that might be connected to weathering and oxidation zone near the surface. Plots of magmatic ferrocolumbite are shown in Figure 10a. A magmatic zircon–thorite solid solution and destabilized thorite, i.e., hydrothermal, can be seen in Figure 10b. Zircon is typically magmatic (Figure 11a), almost fresh with ΣSi + Zr cations equal to two, and finally, Si/Zr ratio < 1.2 (Figure 11b).

8. Conclusions

1. Inside the NW-trending Shear Zone, post-collisional A-type leucogranite is deformed, preserves some magmatic accessories (e.g., columbite, zircon, and thorite), and includes destabilized rare metal-bearing minerals due to hydrothermal alteration.
2. Zircon, with a Si/Zr ratio < 1.2, is the most preserved magmatic accessory. On the other hand, interstitial fluorite and apatite are completely destabilized due to decomposition by hydrothermal fluids at pH = 2–7. Newly formed hydrothermal pyrite indicates destabilization at reducing conditions.
3. Destabilization of fluorite and apatite results in the liberation of Ca^{2+}, Y^{3+}, P^{5+}, F^{-}, and Cl^{-}, which enables the crystallization of new niobates and P-F-rich thorite.
4. The resulting destabilized P-F-rich thorite phases develop in three successive stages. Stages I and II witness the crystallization of Ce-bearing thorite, which is sodic and Si-depleted. In stage III, U-Nb-Y-bearing thorite is Zr-rich, non-sodic, and relatively Si-enriched.
5. Three newly crystallized hydrothermal niobates are formed at the expense of magmatic columbite: fergusonite-Y, petscheckite, and uranopyrochlore. They are U-, Th-, and Y-rich and contain up to 15.24 wt% UO_2, 9.52 wt% ThO_2, and 6.03 wt% Y_2O_3.
6. Based on a proposed paragenetic sequence, ore minerals can be distinguished into magmatic (stabilized), hydrothermal (non-stabilized), and supergene minerals. The latter are the lowest in abundance and comprise goethite, Fe-oxyhydroxide, altered betafite, and altered uranothorite.

Supplementary Materials: The following supporting information can be downloaded at https://www.mdpi.com/article/10.3390/resources14010004/s1. Table S1: Electron microprobe analyses (EMPA) of the investigated rare-metal minerals.

Author Contributions: Conceptualization—A.A.S. and A.M.E.-T.; methodology—A.A.S., A.M.E.-T. and G.M.S.; formal analysis—A.M.E.-T.; original draft, A.A.S. and A.M.E.-T.; writing—A.A.S., A.M.E.-T. and G.M.S.; review and revisions—A.A.S. All authors have read and agreed to the published version of the manuscript.

Funding: This research received no funding from any institution or organization.

Data Availability Statement: Data are contained within the article and Supplementary Materials.

Acknowledgments: The authors thank Sayed M. Omar, Nuclear Materials Authority of Egypt, for his field assistance. They are also indebted to Minghua Ren, Las Vegas, USA, for carrying out the EMPA. Thanks to Hesham Mokhtar and Ahmed Abd El Fatah, Cairo University for drafting some figures.

Conflicts of Interest: The authors declare no competing interests.

References

1. Johnson, P.; Andresen, A.; Collins, A.; Fowler, A.; Fritz, H.; Ghebreab, W.; Kusky, T.; Stern, R. Late Cryogenian-Ediacaran history of the Arabian-Nubian Shield: A review of depositional, plutonic, structural, and tectonic events in the closing stages of the northern East African Orogen. *J. Afr. Earth Sci.* **2011**, *61*, 167–232. [CrossRef]
2. Stern, R.J. Neoproterozoic formation and evolution of Eastern Desert continental crust—The importance of the infrastructure superstructure transition. *J. Afr. Earth Sci.* **2017**, *146*, 15–27. [CrossRef]
3. Mohammad, A.T.; El Kazzaz, Y.A.; Hassan, S.M.; Taha, M.M.N. Neoproterozoic tectonic evolution and exhumation history of transpressional shear zones in the East African Orogen: Implications from kinematic analysis of Meatiq Area, Central Eastern Desert of Egypt. *Int. J. Earth Sci.* **2019**, *109*, 253–279. [CrossRef]
4. Johnson, P.R. The Arabian-Nubian Shield, an introduction: Historic overview, concepts, interpretations, and future issues. In *The Geology of the Arabian-Nubian Shield, Regional Geology Reviews*; Hamimi, A., Fowler, A.R., Liegeois, J.-P., Collins, A., Abdelsalam, M., Abd EI-Wahed, M., Eds.; Springer: Cham, Switherland, 2021; pp. 1–38.
5. Hamimi, Z.; Fowler, A. Najd Shear System in the Arabian-Nubian Shield. In *The Geology of the Arabian Nubian Shield, Regional Geology Reviews*; Hamimi, Z., Fowler, A., Liégeois, J., Collins, A., Abdelsalam, M.G., Abdel Wahed, M., Eds.; Springer: Cham, Switherland, 2021; pp. 359–389.
6. Hamimi, Z.; Hagag, W.; Fritz, H.; Baggazi, H.; Kamh, S. The tectonic map and structural provinces of the Late Neoproterozoic Egyptian Nubian Shield: Implications for crustal growth of the Arabian-Nubian Shield (East African Orogen). *Front. Earth Sci.* **2022**, *10*, 921521. [CrossRef]
7. Raslan, M.F.; El-Feky, M.G. Radioactivity and mineralogy of the altered granites of the Wadi Ghadir shear zone, South Eastern Desert, Egypt. *Chin. J. Geochem.* **2012**, *31*, 30–40. [CrossRef]
8. Shahin, H.A. *Zr-Y-Nb-REE Mineralization Associated with Microgranite and Basic Dykes at EL Sela Shear Zone, South Eastern Desert, Egypt*; Springer Plus: Berlin/Heidelberg, Germany, 2014; Volume 3, p. 573.
9. El-Afandy, A.H.; El-Feky, M.G.; Taha, S.H.; El Minyawi, S.M.; Sallam, H.A.; Ebyan, O.A.; Yousef, E.; Hanfi, M.Y. Natural radionuclide concentrations by γ-ray spectrometry in granitic rocks of the Sol Hamed Area, Southeastern Desert of Egypt, and their radiological implications. *Minerals* **2022**, *12*, 294. [CrossRef]
10. Oraby, A.H.; Saleh, G.M.; Hassan, E.M.; Eldabour, S.E.; El Tohamy, A.M.; Kamar, M.S.; El Feky, M.G.; El Taher, A. Natural radioactivity and radioelement potentiality of mylonite rocks in Nugrus Area, Southeastern Desert, Egypt. *Radiochemistry* **2022**, *64*, 645–655. [CrossRef]
11. Ibrahim, M.E.; Shalaby, M.H.; Ammar, S.E. Preliminary studies on some uranium and thorium bearing pegmatites at G. Abu Dob, Central Eastern Desert, Egypt. *Bull. Egypt. Acad. Sci.* **1997**, *47*, 173–188.
12. Abdalla, H.M.; El Afandy, A.H. Contrasting mineralogical and geochemical characteristics of two A-type pegmatite fields, Eastern Desert, Egypt. *Egypt. Mineral.* **2003**, *15*, 287–328.
13. Abdel Warith, A.; Ali, M.A.; El Balakssy, S.S. Petrology and radioactivity of granitoid rocks at Batuga area, South Eastern Desert, Egypt. In Proceedings of the 6th International Conferences on Geochemistry, Alexandria University, Alexandria, Egypt, 15–16 September 2004; pp. 429–448.
14. Abdel Warith, A.M.; Raslan, M.F.; Ali, M.A. Mineralogy and Radioactivity of pegmatite bodies from the granitic pluton of Gabal Um Taghir El-Tahatani area, Central Eastern Desert, Egypt. In Proceedings of the 10th International Conference on Mining Engineering and Metallurgy, Perth, Australia, 20–22 August 2007; pp. 24–41.
15. Saleh, G.M. Uranium mineralization in the muscovite-rich granites of the Shalatin region, Southeastern Desert, Egypt. *Chin. J. Geochem.* **2006**, *25*, 1–15. [CrossRef]
16. Raslan, M.F.; El-Shall, H.E.; Omar, S.A.; Daher, A.M. Mineralogy of polymetallic mineralized pegmatite of Ras Baroud granite, Central Eastern Desert, Egypt. *J. Mineral. Petrol. Sci.* **2010**, *105*, 123–134. [CrossRef]
17. Abdel Hamid, A.A. Petrography, geochemistry and radioactivity of alkaline A-type granites and associated pegmatites from Gabal Um Guruf region, North Eastern Desert, Egypt. *Egypt. J. Geol.* **2018**, *62*, 283–297.
18. El Mezayen, A.M.; Heikal, M.A.; El-Feky, M.G.; Shahin, H.A.; Abu Zeid, I.K.; Lasheen, S.R. Petrology, geochemistry, radioactivity, and M–W type rare earth element tetrads of El Sela altered granites, south eastern desert, Egypt. *Acta Geochim.* **2019**, *38*, 95–119. [CrossRef]
19. Ali, M.A.; Abdel Gawad, A.E.; Ghoneim, M.M. Geology and mineral chemistry of uranium- and thorium-bearing minerals in rare-Metal (NYF) pegmatites of Um Solimate, South Eastern Desert, Egypt. *Acta Geol. Sin. (Engl. Ed.)* **2021**, *95*, 1568–1582. [CrossRef]
20. Abdel Gawad, A.E. Mineral chemistry aspects of radioactive mineralization associated with Zr-, Nb-, and REE-bearing minerals from felsic dikes at Abu Hawis, North Eastern Desert, Egypt. *Arab J. Geosci.* **2022**, *15*, 791. [CrossRef]
21. Surour, A.A. Sn-W-Ta-Mo-U-REE mineralizations associated with alkali granite magmatism in Egyptian Nubian Shield. In *The Geology of the Egyptian Nubian Shield. Regional Geology Reviews*; Hamimi, Z., Arai, S., Fowler, A.R., El-Bialy, M.Z., Eds.; Springer: Cham, Switherland, 2021; pp. 593–604.

22. Abdalla, H.M.; Matsueda, H.; Saleh, G.M.; Ishihara, S. Phanerozoic rare earth element resources of Egypt: Metallogenetic and mineral exploration constraints. In *The Phanerozoic Geology and Natural Resources of Egypt. Advances in Science, Technology and Innovation*; Hamimi, Z., Khozyem, H., Adatte, T., Nader, F.H., Oboh-Ikuenobe, F., Zobaa, M.K., El Atfy, H., Eds.; Springer: Cham, Switherland, 2023; pp. 581–611.
23. Janeczek, J.; Ewing, R.C. Dissolution and alteration of uraninite under reducing conditions. *J. Nucl. Mater.* **1992**, *190*, 157–173. [CrossRef]
24. Kouske, A.P.; Gerard, M.; Etame, J.; Kanouo, N.S.; Tschouatcha, M.S.; Ghogomu, T.R.; Cuney, M.; Cheo, S.E.; Ngako, V. Paragenesis, mineral chemical and microtextural studies of uranium bearing minerals in the brecciated albitites U-ores from the Kitongo shear zone, Poli region, northern Cameroon. *Int. J. Earth Sci.* **2022**, *111*, 1413–1436. [CrossRef]
25. Saxena, A.; Banerjee, A.; Mitra, N.; Couto, D.S.; Pandey, U.K.; Bisht, B.S.; Sinha, D.K. Comparison of metasomatic and pegmatite type of mineralization in and near Rohil uranium deposit, Sikar District, Rajasthan, India: An insight from field relations, petrography and mineral chemistry. *J. Geol. Soc. India* **2022**, *98*, 1095–1103. [CrossRef]
26. Tomašić, N.; Gajović, A.; Bermanec, V.; Su, D.S.; Rajić Linarić, M.; Ntaflos, T.; Schlögl, R. Recrystallization mechanisms of fergusonite from metamict mineral precursors. *Phys. Chem. Miner.* **2006**, *33*, 145–159. [CrossRef]
27. Frietsch, R. *The Occurrence and Composition of Apatite with Special Reference to Iron Ores and Rocks in Northern Sweden*; Sveriges Geologiska Undersökning: Uppsala, Sweden, 1974; Volume 68, 49p.
28. Bouzari, F.; Hart, C.J.R.; Bissig, T.; Barker, S. Hydrothermal alteration revealed by apatite luminescence and chemistry: A potential indicator mineral for exploring covered porphyry copper deposits. *Econ. Geol.* **2016**, *111*, 1397–1410. [CrossRef]
29. Lorenz, M.; Altenberger, U.; Trumbull, R.B.; Lira, R.; López de Luchi, M.; Günter, C.; Eidner, S. Chemical and textural relations of britholite- and apatite-group minerals from hydrothermal REE mineralization at the Rodeo de los Molles deposit, Central Argentina. *Am. Mineral.* **2019**, *104*, 1840–1850. [CrossRef]
30. Cangelsoni, D.; Broom-Fendley, S.; Banks, D.; Morgan, D.; Yardley, B. Light rare earth element redistribution during hydrothermal alteration at the Okorusu carbonatite complex, Namibia. *Mineral. Mag.* **2020**, *84*, 49–64. [CrossRef]
31. Chowdhury, A.; Lentz, D.R.; Pal, D.C. Hydrothermal alteration and elemental mass balance for the Sudra Copper Deposit, Singhbhum Shear Zone, Eastern India: Implications for both copper and magnetite-apatite mineralization. *Geochem. Explor. Environ. Anal.* **2024**, *24*, geochem2024-004. [CrossRef]
32. Stern, R.J.; Hedge, C.E. Geochronological and isotopic constraints on Late Precambrian crustal evolution in the Eastern Desert of Egypt. *Am. J. Sci.* **1985**, *285*, 97–127. [CrossRef]
33. El Ramly, M.F.; Greilling, R.O.; Kröner, A.; Rashwan, A.A. *On the Tectonic Evolution of the Wadi Hafafit Area and Environs. Eastern Desert of Egypt*; Bulletin of the Faculty of Earth Sciences, King Abdulaziz University: Jeddah, Saudi Arabia, 1984; Volume 6, pp. 113–126.
34. El Ramly, M.F.; Greiling, R.O.; Rashwan, A.A.; Rasmy, A.H. Explanatory note to accompany the geological and structural maps of Wadi Hafafit area, Eastern Desert of Egypt. *Geol. Surv. Egypt* **1993**, *68*, 53.
35. El Gaby, S.; List, F.K.; Tehrani, R. Geology, evolution and metallogenesis of the Pan-African belt in Egypt. In *The Pan-African Belt of Northeast Africa and Adjacent Areas*; El Gaby, R., Greiling, O.R., Eds.; Friedrich Vieweg und Sohn, Braunschweig: Wiesbaden, Germany, 1988; pp. 17–68.
36. Greiling, R.O.; Abdeen, M.M.; Dardir, A.A.; El Akhal, H.; El Ramly, M.F.; El Din Kamal, G.M.; Osman, A.F.; Rashwan, A.A.; Rice, A.H.N.; Sadek, M.F. A structural synthesis of the Proterozoic Arabian-Nubian Shield in Egypt. *Geol. Rundsch.* **1994**, *83*, 484–501. [CrossRef]
37. Fowler, A.; Osman, A.F. The Sha'it-Nugrus shear zone separating Central and South Eastern Deserts, Egypt: A post-arc collision low-angle normal ductile shear zone. *J. Afr. Earth Sci.* **2009**, *53*, 16–32. [CrossRef]
38. Ibrahim, W.S.; Mostafa, M.S.; Ibrahim, M.E.; Watanabe, K.; Soliman, F.A. Deformation history of Nugrus-Sikait belt, south Eastern Desert, Egypt: Implication for tectonic environment. *Int. Res. J. Geol. Min. (IRJGM)* **2014**, *4*, 84–100.
39. El Shaib, G.B.; Radwan, A. Mineralogical and geochemical aspects of garnet bearing S-type granite, Wadi Nugrus, south Eastern Desert, Egypt. *Aswan Univ. J. Environ. Stud.* **2024**, *5*, 372–395. [CrossRef]
40. Saleh, G.M. *Geological Survey and Field Mapping of the Wadi Nugrus-Wadi el Nom Area. The Abu Rusheid Project for the Exploration of Radioactive Mineralization*; Internal Report; Nuclear Materials Authority of Egypt: Cairo, Egypt, 2014.
41. El-Gaby, S. Architecture of the Egyptian Basement Complex. In Proceedings of the Fifth International Conference on Basement Tectonics, Cairo, Egypt, 16–18 October 1983; International Basement Tectonics Association: Oak Ridge, TN, USA, 1983.
42. Khudeir, A.A.; El-Gaby, S.; Kamal El Din, G.M.; Asran, A.M.; Greiling, R.O. The pre-Pan-African deformed granite cycle of the Gabal El-Sibai swell, Eastern Desert, Egypt. *J. Afr. Earth Sci.* **1995**, *21*, 395–406. [CrossRef]
43. Mokhtar, H.; Surour, A.A.; Azer, M.K.; Ren, M.; Said, A. Petrogenesis and possible fingerprints of the Najd shear system on the evolution of deformed granitic rocks in the west Wadi Nugrus area, Egypt. *J. Afr. Earth Sci.* **2023**, *207*, 105045. [CrossRef]

44. Azer, M.K.; Abuamarah, B.A.; Srour, M.M.; Wilde, S.A.; Gomaa, R.M. Mineralogy, geochemistry, and petrogenesis of post-collisional granites from the Arabian-Nubian Shield: Case study from the Gabal Nugrus area in the South Eastern Desert of Egypt. *J. Geol.* 2024, *in press*.
45. Surour, A.A. Medium- to high-pressure garnet-amphibolites from Gebel Zabara and Wadi Sikait, south Eastern Desert, Egypt. *J. Afr. Earth Sci.* **1995**, *21*, 443–457. [CrossRef]
46. Warr, L.N. IMA—CNMNC approved mineral symbols. *Mineral. Mag.* **2021**, *85*, 291–320. [CrossRef]
47. El-Bialy, M.Z. Precambrian Basement Complex of Egypt. In *The Geology of Egypt*; Hamimi, Z., El-Barkooky, A., Friás, J.M., Fritz, H., Abd El-Rahman, Y., Eds.; Springer: Cham, Switherland, 2020; pp. 37–72.
48. Azer, M.K.; Abdelfadil, K.M.; Ramadan, A.A. Geochemistry and petrogenesis of Late Ediacaran rare-metal albite granite of the Nubian Shield: Case study of Nuweibi intrusion, Eastern Desert, Egypt. *J. Geol.* **2019**, *127*, 665–689. [CrossRef]
49. Abuamarah, B.A. Genesis and petrology of post-collisional rare-metal-bearing granites in the Arabian Shield: A case study of Aja ring complex, Northern Saudi Arabia. *J. Geol.* **2020**, *128*, 131–156. [CrossRef]
50. Moghazi, A.M.; Hassanein, M.A.; Mohamed, F.H.; Ali, S. Late neoproterozoic strongly peraluminous leucogranites, south Eastern Desert, Egypt—Petrogenesis and geodynamic significance. *Mineral. Petrol.* **2004**, *81*, 19–41. [CrossRef]
51. Abd El-Naby, H.H.; Frisch, W. Geochemical constraints from the Hafafit Metamorphic Complex (HMC): Evidence of Neoproterozoic back-arc basin development in the central Eastern Desert of Egypt. *J. Afr. Earth Sci.* **2006**, *45*, 173–186. [CrossRef]
52. Heikal, M.T.S.; Khedr, M.Z.; Abd El Monsef, M.; Gomaa, S.R. Petrogenesis and geodynamic evolution of Neoproterozoic Abu Dabbab albite granite, central Eastern Desert of Egypt: Petrological and geochemical constraints. *J. Afr. Earth Sci.* **2019**, *158*, 103518. [CrossRef]
53. El-Bialy, M.Z.; Omar, M.M. Spatial association of Neoproterozoic continental arc I-type and post-collision A-type granitoids in the Arabian-Nubian Shield: The Wadi Al-Baroud Older and Younger Granites, North Eastern Desert, Egypt. *J. Afr. Earth Sci.* **2015**, *103*, 1–29. [CrossRef]
54. Whalen, J.B.; Currie, K.L.; Chappell, B.W. Atype granites: Geochemical characteristics, discrimination, and petrogenesis. *Contrib. Mineral. Petrol.* **1987**, *95*, 407–419. [CrossRef]
55. Eby, G.N. The A-type granitoids. A review of their occurrence and chemical characteristics and speculations on their petrogenesis. *Lithos* **1990**, *26*, 115–134. [CrossRef]
56. Eby, G.N. Chemical subdivision of the A-type granitoids: Petrogenetic and tectonic implications. *Geology* **1992**, *20*, 641–644. [CrossRef]
57. Černý, P.; Ercit, T.S. The classification of granitic pegmatites revisited. *Can. Mineral.* **2005**, *43*, 2005–2026. [CrossRef]
58. Černý, P. Rare-element granitic pegmatites. Part 1: Anatomy and internal evolution of pegmatite deposits. Part 2: Regional to global environments and petrogenesis. *Geosci. Can.* **1991**, *18*, 49–81.
59. Omar, S.A.M. Geology and Geochemical Features of the Radioactive Occurrences of Um-Anab Granitic Masses, Eastern Desert, Egypt. Master's Thesis, Cairo University, Cairo, Egypt, 1995; 195p.
60. El-Sayed, M.M. The Neoproterozoic Dubr intrusives, Central Eastern Desert, Egypt: Petrological and geochemical constraints on the evolution of a mafic-felsic suite. *Mineral. Geochem.* **2003**, *179*, 1–42. [CrossRef]
61. El-Sayed, A.M.; Assran, H.M.; Abu Eltta, A. Petrographic, radiometric and paleomagnetic studies for some alkaline rocks, South Nusab El Balgum Mass Complex, South Western Desert, Egypt. *Geomaterials* **2014**, *4*, 27–46. [CrossRef]
62. Fawzy, M.F.; Mahdy, N.M.; Sami, M. Mineralogical characterization and physical upgrading of radioactive and rare metal minerals from Wadi Al-Baroud granitic pegmatite at the Central Eastern Desert of Egypt. *Arab. J. Geosci.* **2020**, *13*, 413. [CrossRef]
63. Abdel Gawad, A.E. Mineral chemistry (U, Th, Zr, REE) in accessory minerals from Wadi Rod Elsayalla granitoids, South Eastern Desert, Egypt. *Arab. J. Geosci.* **2021**, *14*, 1996. [CrossRef]
64. Černý, P.; Ecrit, T.S. Some recent advances in the mineralogy and geochemistry of Nb and Ta in rare-element granitic pegmatites. *Bull. Mineral.* **1985**, *108*, 499–532. [CrossRef]
65. Černý, P. Characteristics of pegmatite deposits of tantalum. In *Lanthanides, Tantalum, and Niobium*; Möller, P., Ed.; Springer: Berlin/Heidelberg, Germany, 1989; pp. 195–239.
66. Breiter, K.; Förster, H.-J.; Škoda, R. Extreme P-, Bi-, Nb-, Sc-, U- and F-rich zircon from fractionated perphosphorous granites: The peraluminous Podlesí granite system, Czech Republic. *Lithos* **2006**, *88*, 15–34. [CrossRef]
67. Förster, H.-J. Composition and origin of intermediate solid solutions in the system thorite-xenotime-zircon-coffinite. *Lithos* **2006**, *88*, 35–55. [CrossRef]
68. Hoskin, P.W.O.; Schaltegger, U. The composition of zircon and igneous and metamorphic petrogenesis. *Rev. Mineral. Geochem.* **2003**, *53*, 27–62. [CrossRef]
69. Mahdy, N.M. Textural and chemical characteristics of zircon, monazite, and thorite, Wadi Al-Baroud area, Eastern Desert of Egypt: Implication for rare metal pegmatite genesis. *Ore Geol. Rev.* **2021**, *136*, 104225. [CrossRef]
70. Linnen, R. The solubility of Nb–Ta–Zr–Hf–W in granitic melts with Li and Li-F: Constraints for mineralization in rare-metal granites and pegmatites. *Econ. Geol.* **1998**, *93*, 1013–1025. [CrossRef]

71. Migdisov, A.A.; Williams-Jones, A.E. An experimental study of the solubility and speciation of neodymium (III) fluoride in F-bearing aqueous solutions. *Geochim. Cosmochim. Acta* **2007**, *71*, 3056–3069. [CrossRef]
72. Migdisov, A.A.; Williams-Jones, A.E.; Wagner, T. An experimental study of the solubility and speciation of the rare earth elements (III) in fluoride and chloride-bearing aqueous solutions at temperatures up to 300 °C. *Geochim. Cosmochim. Acta* **2009**, *73*, 7087–7109. [CrossRef]
73. London, D. Pegmatites. In *The Canadian Mineralogist*; Special Publication No. 10; Mineralogical Society of America: Chantilly, VA, USA, 2008; 347p.
74. London, D. The origin of primary textures in granitic pegmatites. *Can. Mineral.* **2009**, *47*, 697–724. [CrossRef]
75. Dingwell, D.B.; Hess, K.U.; Knoche, R. Granite and granitic pegmatite melt: Volumes and viscosities. *Trans. R. Soc. Edinb. Earth Sci.* **1996**, *87*, 65–72.
76. Salvi, S.; Williams-Jones, A.E. Alkaline granite-syenite deposits. In *Rare-Element Geochemistry and Mineral Deposits*; Geological Association of Canada Short Course Notes; Linnen, R.L., Samson, I.M., Eds.; Geological Association of Canada: St. John's, NL, Canada, 2004; Volume 17, pp. 315–341.
77. Hawthorne, F.C. Structure and chemistry of phosphate minerals. *Mineral. Mag.* **1998**, *62*, 141–164. [CrossRef]
78. Valsami-Jones, E. Phosphate Minerals—An Overview. Volume 1 Mineralogy/Non-silicates. In *Encyclopedia of Geology*, 2nd ed.; Alderton, D., Elias, S.A., Eds.; Academic Press: Cambridge, MA, USA; Elsevier Ltd.: Amsterdam, The Netherlands, 2021; pp. 422–427.
79. Christoffersen, J.; Christoffersen, M.R.; Kjaergaard, N. The kinetics of dissolution of calcium hydroxyapatite in water at constant pH. *J. Cryst. Growth* **1978**, *43*, 501–511. [CrossRef]
80. Valsami-Jones, E.; Ragnarsdottir, K.V.; Putnis, A.; Bosbach, D.; Kemp, A.J.; Cressey, G. The dissolution of apatite in the presence of aqueous metal cations at pH 2–7. *Chem. Geol.* **1998**, *151*, 215–233. [CrossRef]
81. Brown, J.L. Calcium phosphate precipitation—effects of common and foreign ions on hydroxy-apatite crystal growth. *Soil Sci. Soc. Am. J.* **1981**, *45*, 482–486. [CrossRef]
82. Moine, B.; Salvi, S. Role of fluorine-rich fluids in the hydrothermal transport of "immobile" elements (Th, Zr, REE). *Bull. Deliaison Soc. Fr. Mineral. Cristallogr. (SFMC)* **1999**, *11*, 90–92.
83. Abd El-Naby, H. Role of argillic alteration in uranophane precipitation along shear zones of the Gattar granites, Eastern Desert, Egypt. *J. King Abdulaziz Univ. Earth Sci.* **2009**, *20*, 45–69. [CrossRef]
84. Abd El-Naby, H.H. High and low temperature alteration of uranium and thorium minerals, Um Ara granites, south Eastern Desert, Egypt. *Ore Geol. Rev.* **2009**, *35*, 436–446. [CrossRef]
85. Dawood, Y.H.; Abd El-Naby, H.H. Genesis of uranyl mineralization in the Arabian Nubian Shield: A review. *J. Asian Earth Sci.* **2022**, *225*, 105047. [CrossRef]
86. Mücke, A.; Strunz, H. Petscheckite and liandratite, two new pegmatite minerals from Madagascar. *Am. Mineral.* **1978**, *63*, 941–946.
87. Tomašić, N.; Raade, G.; Bermanec, V. REE-bearing petscheckite from Tiltvika, Nordland, Norway, and its heating products. *Neues Jahrb. Mineral.-Monatshefte* **2004**, *4*, 163–175. [CrossRef]
88. Melcher, M.; Graupner, T.; Gäbler, H.E.; Sitnikova, M.; Henjes-Kunst, F.; Oberthür, T.; Gerdes, A.; Dewaele, S. Tantalum–(niobium–tin) mineralisation in African pegmatites and rare metal granites: Constraints from Ta–Nb oxide mineralogy, geochemistry and U–Pb geochronology. *Ore Geol. Rev.* **2015**, *64*, 667–719. [CrossRef]
89. Zhang, L.; Wang, F.; Zhou, T.; Chen, Z.; Du, X.; Zhang, S. The origin of uranium deposits related to the Huangmeijian A-type granite from the Lu-Zong volcanic basin, South China: Constraints from zircon U-Pb geochronology and mineral chemistry. *Ore Geol. Rev.* **2022**, *141*, 104665. [CrossRef]